Interactive Patient-Customized Curvilinear Reformatting for Improving Neurosurgical Planning

Wu, Shin-Ting[a,c], Wallace Souza Loos[a,c], Dayvid Leonardo de Castro Oliveira[b], Fernando Cendes[b,c], Clarissa L. Yasuda[b,c] and Enrico Ghizoni[b,c]

[a]*School of Electrical and Computer Engineering*; [b]*School of Medical Sciences, University of Campinas*, [c]*BRAINN Research, Innovation and Dissemination Center of the University of Campinas Campinas, Brazil*

Abstract

Purpose Visualizing a brain in the native space while preserving the superficial cerebral veins and surrounding regions for context plays an essential role in neurosurgical planning. This paper presents a visualization tool promoting this kind of perception from single gadolinium contrast-enhanced T1-weighted magnetic resonance imaging of a non-defective and non-resective skull.

Method The curvilinear reformatting tool on the supratentorial compartment is applied to peel off the tissues to the depth of the dura-mater, revealing the cortical and vascular spatial relationships. The major advantage of our proposed tool over the known one is that co-registration of anatomical and vascular volumes is not required.

Results The reliability of the technique is demonstrated through comparisons between preoperative images and digital photos of brain cortical surface after the removal of the dura-mater of 20 patients underwent surgery in the Clinics Hospital of the University of Campinas from January 2017 to April 2018.

Conclusion Single fat-suppressed GAD-contrast enhanced T1-weighted magnetic resonance scans can provide accurate preoperative 3D views of cortical and vascular relationships similar to the neurosurgeons' intraoperative views. In developing countries, where the access to state-of-the-art health technology is not always available, these views may improve the safety of complex neurosurgery.

Keywords: Neurosurgical planning; curvilinear reformatting; exploratory visualization; vascular landmarks.
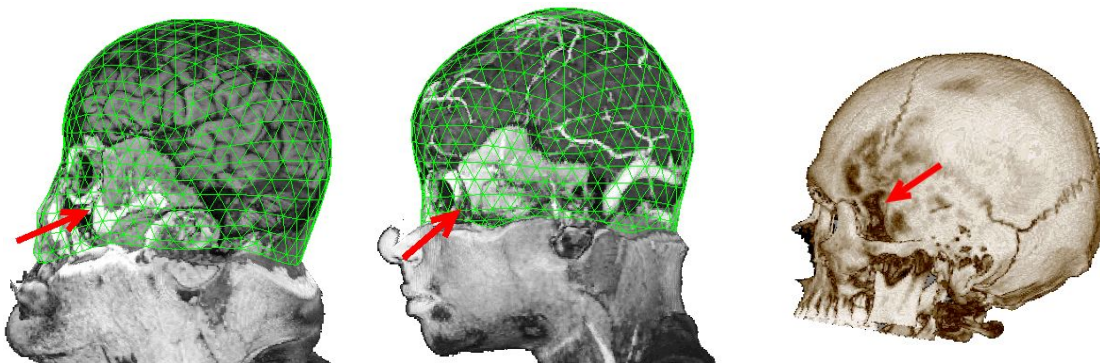
Introduction

Subtle lesions near eloquent brain areas are not always evident on the craniotomy field even with a neuronavigation system, creating uncertainties for neurosurgeons to perform minimally invasive safe resection. Neuroanatomy recognition under the surgical field is greatly helped by preoperative planning using the relations between superficial veins and cortical anatomy [11,14]. Computed tomography angiography or venography

Corresponding author: Wu Shin-Ting, ting@dca.fee.unicamp.br . Av. Albert Einstein - 400, Cidade Universitária Zeferino Vaz, Campinas, São Paulo, Brazil, Zip code: 13083-852

(CTA/CTV), magnetic resonance angiography or venography (MRA/MRV), and digital subtraction catheter angiography (DSCA), in conjunction with anatomical magnetic resonance imaging, have been used by surgery groups [2,3,10]. Accurate co-localization of vascular and cortical anatomy is, however, a concern. Once both brain parenchyma and gadolinium-enhanced vessels have higher MR signal intensity, this paper presents a technique to visualize the spatial relation of the superficial veins and the supratentorial cortical anatomy from gadolinium-enhanced T1-weighted magnetic resonance volumes available in the Clinics Hospital of the University of Campinas (Unicamp-HC).

Starting point is the patient-customized dura-mater oriented curvilinear (multiplanar) reformatting (CMPR) technique proposed in [8], since their outermost peeling layer approaches the internal table of calvaria in T1-weighted magnetic resonance scans. Originally proposed by Bastos et al. [1], CMPR consists of peeling off the layers of the brain with a mesh constructed from manually delineated brain contours on a series of 2D aligned images. It is time-consuming and error-prone. On top of image processing foundations, several non-brain removal algorithms have been proposed to implicitly get the brain cortical surface [6,7,13]. Nevertheless, the non-brain fiducial landmarks, such as the veins, are removed in these techniques, impairing craniotomy planning.

Back to the mesh approach, Wu et al. [18] devised a less laborious way to input a mesh. Instead of delineating the surface of interest per slice, a user draws it directly on a 3D scalp. Loos et al. [8] further reduce the number of interactions using a semi-automatically generated parametric mesh. Although their procedure was designed to T1-weighted magnetic resonance imaging (T1wMRI) 3D sequences (Fig. 1(a)), we conjectured peeling off the layers of the brain from T1-weighted fat-suppressed gadolinium-contrast enhanced magnetic resonance imaging (GAD-T1wMRI) 3D sequences (Fig. 1(b)) to the depth of the pia mater should make visible both vascular and cortical anatomy. This is because contrast-enhanced superficial cerebral veins are attached to the pia mater of the gyri.

Validation tests showed, however, the procedure proposed by Loos et al. failed to reveal the temporal lobes as indicated by the red arrows in Fig. 1. A careful analysis led us to perceive that the shallow depression of temporal fossa on the side of the calvaria (Fig. 1(c)) is overlooked. For correctly exposing temporal lobes and middle cerebral veins, we should further deepen the cropping mesh towards the brain in the temporal fossa.

Fig. 1: A dura-mater adhering mesh (in green) proposed in [7] can reveal the cortical surface of either (a) a T1wMRI or (b) a GAD-T1wMRI sequences except the temporal lobes indicated by the red arrows. The depression in the temporal fossa, indicated by an arrow in (c) a computed tomography scan is neglected.

From the technological view, the major contributions of our work are: (1) the way the depression in the temporal fossa can be roughly segmented, and (2) the way we improve the shape of the cortical envelope proposed in [8] to completely uncover the vascular and cortical structures inside the cranial vault and on the supratentorial compartment.

Materials and methods

The key ideas presented in [8] are applied. First, to remove the background noise of the raw data (Figure 4(a)) using a threshold ζ proposed in [17] for preserving all samples along the view direction and behind the scalp (Figure 4(b)). Second, to explore the feature of T1wMR images for distinguishing the dura-mater. Third, to apply the Gaussian smoothing filter for reducing the number of irrelevant subtle transitions between the scalp and the skull. Fourth, to build a parametric triangular mesh for bridging the samples of the raw data and the user's spatial mental model. Finally, to use the dura-mater as the reference for constructing this parametric triangular mesh. To take into account the shallow depression in the temporal fossa, we faced two challenging issues: to differentiate the signal intensity variations in the temporal fossa from the signal variations over the facial skeleton and the skull base; and to distinguish the signal transition between the skull and the CSF among a variety of tissues that fill the temporal fossa and its vicinity.

Materials

Two groups of T1wMR scans were used. The first group, comprising 511 subjects classified into the age-subgroups 11-20, 21-30, 31-40, 41-50, 51-60, 61-70, 71-80, and 81-90, was used for validating the viewing of the brain anatomy. The second group, consisting of GAD-T1wMR sequences of 20 operated patients in the Unicamp-HC from January 2017 to April 2018, allowed us to comparatively assess the quality of the preoperative view of cortical and vascular relationships provided by our proposal with respect to the neurosurgeons' intraoperative view. All T1wMR sequences from the Unicamp-HC were acquired in a 3T MRI scanner (Philips Medical Systems, Best, The Netherlands). The acquisition parameters were: voxel size $=1\times1\times1$ mm^3, no gap, TR=7

ms, TE=3.2 ms, flip angle = 8, matrix =240x240, FOV=240x240, and resolution=180x240x240.

Image Analysis: Calvarial Signal Intensity Variation Patterns

We shot a ray in the normal direction of the mesh at each vertex sample on a T1wMR volume and analyzed the signal intensity variations at discrete steps of voxel dimensions [8]. In our experiments, we fixed the step size in 1mm and a Gaussian mask in the size of 9 voxels $\times$ 9 voxels $\times$ 9 voxels ($\delta = 2$). The threshold ζ was configured interactively per patient with use of a slider.

Fig. 2(a) illustrates the sagittal view of a filtered volume. Shooting a ray from any vertex in the rounded portion of the calvaria and sampling the intensity values at uniformly spaced points (Fig. 2(a)), the global minimum occurs between a sample of the scalp (about 10mm) and a sample of the brain (about 40mm) (Fig. 2(b)). The corresponding sample of this minimum is in the vicinity of dura-mater that surrounds the subarachnoid space filled by the CSF of the lowest signal intensity. This finding agrees with the results reported in Huempfner-Hierl et al. [5] that the distance between the scalp and the skull and the scalp thickness are almost the same in the high-rounded skullcap. The exception are skull defects or abnormalities that are not considered in this work.
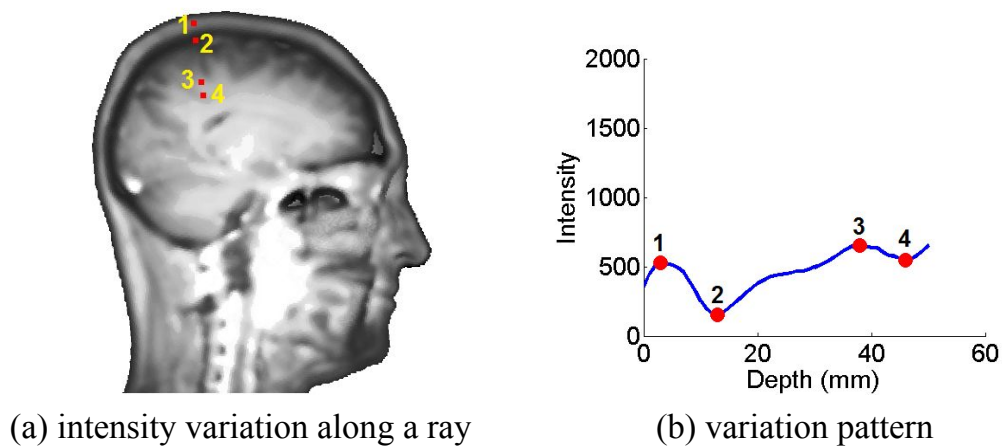

(a) intensity variation along a ray   (b) variation pattern

Fig. 2: Intensity samples along (a) a crossing rounded skullcap ray (samples in red) and (b) the corresponding signal intensity $\times$ depth (mm) plot with the global minimum at "2". .

In the temporal fossa, the rays may cross the zygomatic bone (intermediate signal intensity) and the temporalis muscle (intermediate signal intensity) mingled with fat pad (high signal intensity), yielding different variation patterns. We conducted the same investigation presented in [8] for distinguishing characteristic variation patterns in the temporal fossa. We collected the signal intensities along rays shot from the vertices highlighted in Fig. 3(a) in the depth range of [0,50]mm from the scalp (Fig. 3(b)), and manually separated them into five classes: the outermost rays in blue, the interior rays in

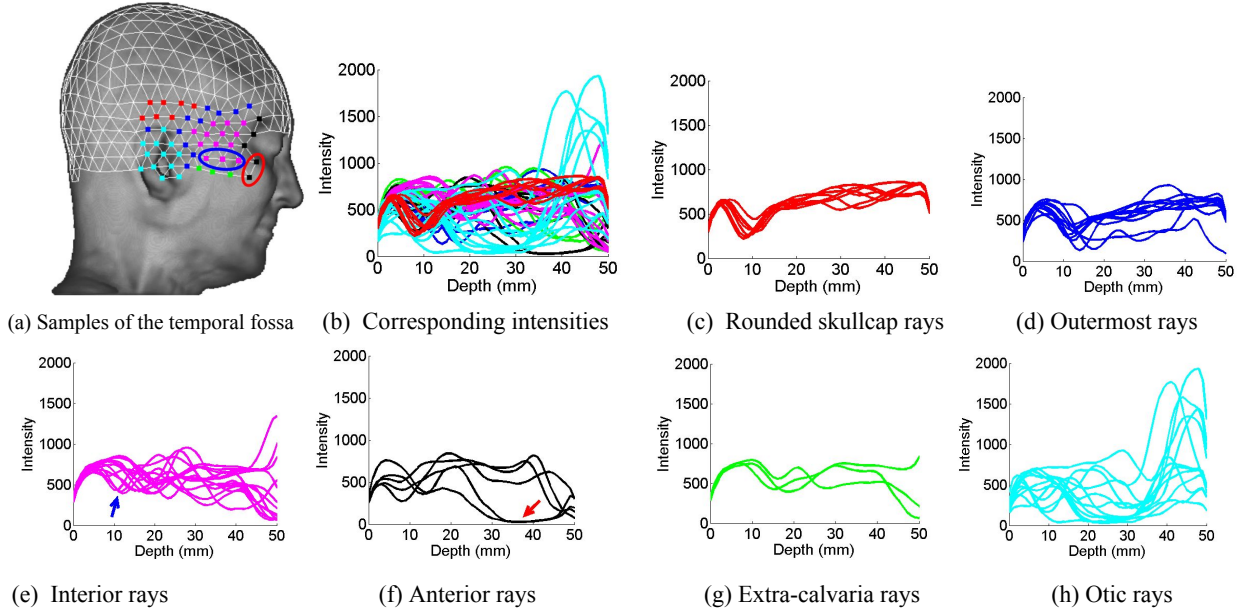magenta, the anterior rays in black, the extra-calvaria rays in green, and the otic rays in cyan.

(a) Samples of the temporal fossa   (b) Corresponding intensities   (c) Rounded skullcap rays   (d) Outermost rays

(e) Interior rays   (f) Anterior rays   (g) Extra-calvaria rays   (h) Otic rays

Fig. 3: Intensity variation patterns in the temporal fossa and its vicinity: (a) samples, (b) signal intensity $\times$ depth (mm) graphs along the corresponding rays, and segmentation into (c) the rounded skullcap rays, (d) outermost rays, (e) interior rays, (f) anterior rays, (g) extra-calvaria rays, and (h) otic rays.

The signal variation pattern of the outermost rays (Fig. 3(d)), closest to the elevated border of the temporal fossa, is similar to the rays shot from the red vertices on the rounded skullcap drawn in Fig. 3(c). Only the global minimum, corresponding to the CSF, is located slightly deeper because of a thin layer of the temporalis muscle along the ray.

The intensity variation pattern of the interior rays is such a one that the depth of the global minimum (CSF) varies gradually, accompanying the shape of the shallow depression of the temporal fossa as depicts Fig. 3(e). In our evaluation with 511 test volumes, the greatest depth is not larger than three times the depth of the global minimum of the outermost rays. Note that there are rays with a valley at the depth shallower than the global minimum of the outermost rays, as indicated by the blue arrow in Fig. 3(e). The corresponding samples circled in blue in Fig. 3(a) are on the zygomatic arch, which Hamid et al. [4] showed to be a reliable landmark of the middle fossa dura-mater.

The anterior rays, which cross the sphenozygomatic suture, present the global minimum at even greater depth (Fig. 3(f)). Note that the rays may cross the CSF inside the skull vault without touching the brain. In this case, we have, instead of a point, an interval of values around the global minimum in the per-ray intensity $\times$ depth graph, as indicated by the red arrow in Fig. 3(f). The corresponding samples of these rays are circled in red in Fig. 3(a).

The extra-calvaria rays cross the face muscle and tissue below the skull base of the supratentorial compartment. They may cross a variety of face soft tissues, presenting several high-low transitions in intensity × depth graphs as shown in Fig. 3(g). Nevertheless, there is always a high-low transition corresponding to the transition from the tissues of higher intensities to a structure involving the CSF (the lowest intensity) in a deeper layer.

The otic rays present a very irregular behavior due to external ears, bony and cartilaginous external auditory canal, and their adjacent structures. Although most of these rays are under the skull base of the supratentorial compartment and do not cross the brain, we observe that when a ray crosses the CSF there is always a high-to-low transition. The higher signal intensities at the right endpoint of graphs presented in Fig. 3(h) correspond, in fact, to the brain stem.

An Implementation

If we can describe the MRI signal intensity as a scalar continuous function $F(x,y,z)$ over a spatial head domain, we can model the dura-mater as a structure that lies in the vicinity of the isosurface $F(x,y,z) = m$, where m is the global minimum. The distance of this isosurface to the scalp is less than three times the depth of the global minimum of the outermost rays. What we have are, however, discrete samples of $F(x,y,z)$. We propose to estimate the wanted isosurface by fitting to these samples a parametric spherical mesh with the radius equal to 55% of the largest dimension of a ζ-threshold-based filtered T1wMR volume and the center at $\overline{C} = \frac{\sum_{i=1}^{n} P_i}{n}$, where P_i are position coordinates of all n valid head voxels (Fig. 4(c)). An overview of our proposed pipeline, from the raw data to uncovered cortical and vascular structures, is presented in Fig. 4. Algorithmically, we divide the procedure in three stages: (1) towards the scalp (Figure 4(e)), (2) towards the rounded dura-mater (Figure 4(f)), and (3) towards the temporal fossa (Figure 4(h)).
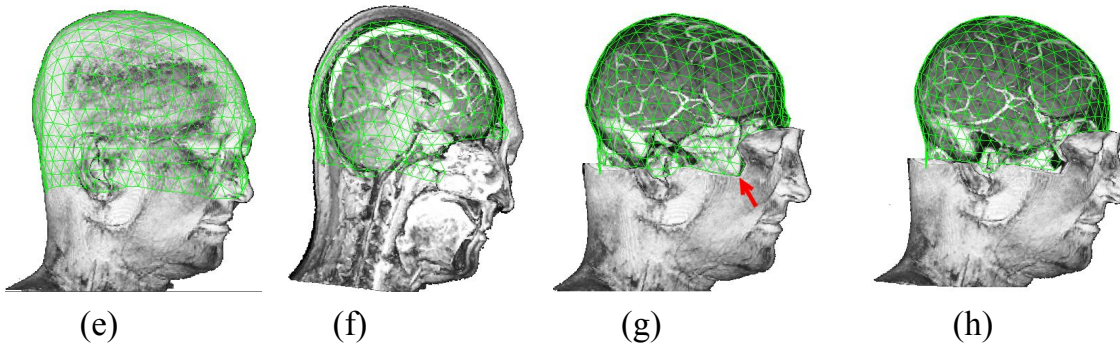

(a)   (b)   (c)   (d)

| (e) | (f) | (g) | (h) |
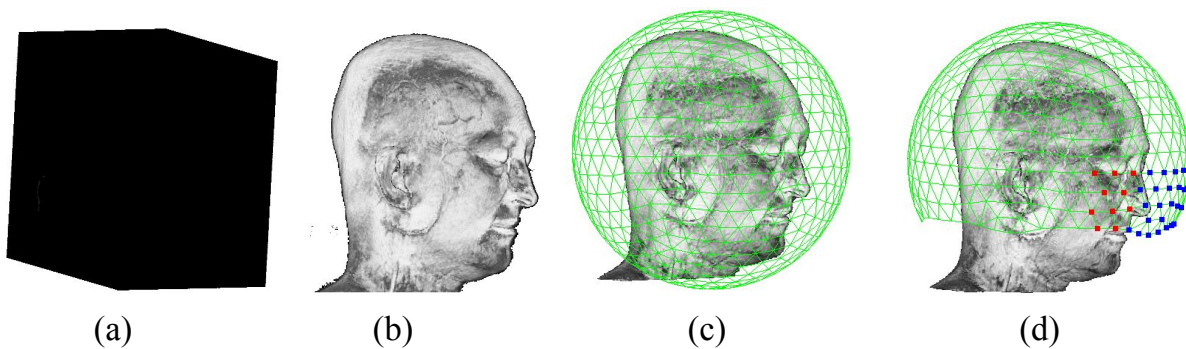
Fig. 4: Cortical envelope modeling pipeline: (a) raw data, (b) filtered data, (c) parametric spherical mesh, (d) parametric hemispherical mesh with estimated vertices over facial skeleton (in blue) and over temporal fossa (in red), (e) scalp envelope, (f) non-smoothed cortical envelope, (g) smoothed extra-temporal cortical envelope with covered temporal fossa indicated by the red arrow, and (h) full cortical envelope.

User interactions

User should interactively select a clipping plane above which the brain should be uncovered, and provide two points, one on the scalp and another on the cortical surface of the temporal lobe for configuring the maximum depth of dura-mater from the scalp in the rounded skullcap. The clipping plane limits the scope of cases that the algorithm can correctly deal with (Figure 4(d)) and, the depth value prevents from falling into an endless search loop if a ray goes through a sulcus. For dealing with temporal fossa, we propose to place the clipping plane at the height of the middle fossa skull base (at the level of the tragus) (Fig. 5(a)), and to estimate the depth of dura-mater at the height of the top of the external ear (at the level of the temporal line) (Fig. 5(b)).

To roughly determine the parametric intervals of the facial skeleton and the seed of the temporal fossa (Fig. 7(a)), user should also choose two lateral epicanthi (Fig. 5(c)). The lateral epicanthus is related to the zygomatic bone which is the anterior boundary of the temporal fossa, and the zygomatic bone is, its turn, connected to the zygomatic arch, the inferior boundary of the temporal fossa, and linked to the greater wing of the sphenoid bone (part of the skull base). This neuroanatomy knowledge allows us to consider that the vertices in the outer direction of the lateral epicanthus of each eye side are over the temporal fossa. In Fig. 4(d) these vertices are highlighted in red.
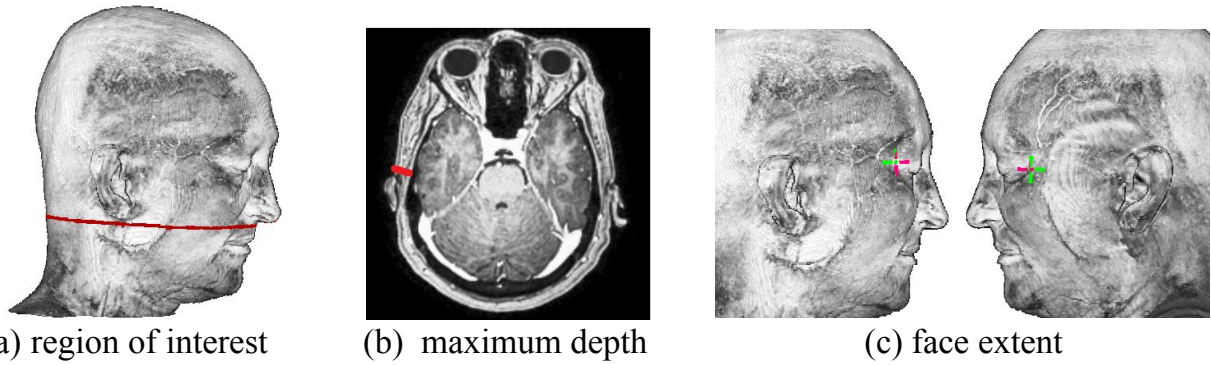
| (a) region of interest | (b) maximum depth | (c) face extent |

Fig. 5: Required user input highlighted in red: (a) clipping plane, (b) two extreme points of a segment corresponding approximately to the maximum depth of the rounded skullcap, and (c) the lateral epicanthi.

Mesh Deforming

In the first and the second deformation stages, the same procedure presented in [8] is carried out. In the first stage, each vertex is uniformly displaced in the opposite direction of its normal vector until it reaches a sample with an intensity value above the threshold ζ. Then, in the second stage, this scalp fitted mesh cap (SFM) is further pushed inward a ray of length of 50mm in the direction of the normal vector until the minimum of the signal intensities (intensity condition) or the user-defined maximum depth (depth condition) is reached [8]. At the end of this stage, the mesh cap fitting the dura-mater in almost the whole extent of the cortical surface, except in the temporal fossae, is built (Fig. 4(f)). This dura-mater adhering mesh always cuts the border of the temporal fossa characterized by the brighter intensity in T1wMR sequences, as indicates the red arrow in Fig. 6.
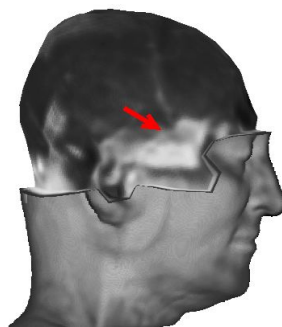

Fig. 6: Brighter border corresponding to the intersection of the dura-mater adhering mesh and the temporal line in a smoothed T1wMR volume.

In the third stage the smoothed rounded skullcap dura-mater adhering mesh, rDAM (Fig. 4(g)), is further deformed by locally adjusting the vertices that are inside the region bounded by the brighter border. There are two issues to be concerned. First, we should

identify the vertices of rDAM that lie in the temporal fossae. Second, it is necessary to displace these vertices to a dura-mater in the supratentorial compartment.

For the first issue, we use the brighter border of the temporal fossa. In the vicinity of this brighter border, even the vertices lie closer to the dura-mater, they could be stopped by the depth condition due to numerical roundings. Hence, we revisit all vertices stopped by this condition and check whether there is a global minimum lying in the neighborhood of 3mm. If it is the case, we displace the vertex to the corresponding minimum intensity and re-tag it as "extra-temporal". As a result, all vertices in the temporal fossa are correctly tagged as "temporal". We proceed with discarding the extra-temporal vertices that were also stopped by the depth condition. We recurrently insert adjacent triangles of the seed triangle inside the temporal fossa (Fig. 7(a)) until all the connected triangles with brighter signals[1] are reached. In Fig. 7(b), vertice of brighter triangles are highlighted in blue. All these vertices are tagged as "temporal". Nevertheless, the rays shot from the vertices on the temporal fossa should cross the calvaria at the depth not larger than three times the maximum depth [4]. Therefore, we revisit the "temporal" vertices and retag the ones that do not satisfy this second condition as "undecidable".
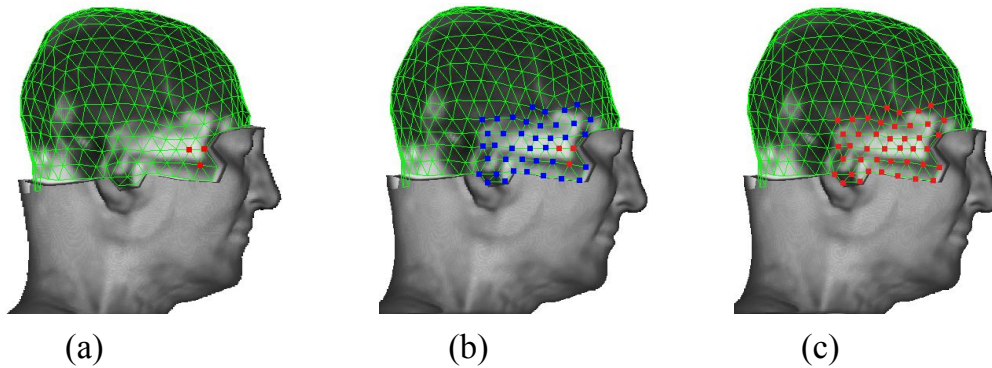

| (a) | (b) | (c) |

Fig. 7: Retagging the samples after dura-mater fitting according to the bright border of the temporal fossa: (a) initial tagged samples in red, (b) recurrently inserted untagged candidates in blue, and (c) newly tagged samples in red.

For the second issue, we simply displace the vertices tagged as "temporal" and the ones on the zygomatic bone (associated to the anterior rays) to the global minimum of the signal intensity along each ray in the range of [0,50]mm and recalculate the positions of "undecidable" vertices in such a way that the triangles to which they belong are almost coplanar with respect to their neighbouring triangles. In this way we preserve the smoothness of rDAM on its border. Fig. 4(h) presents the final dura-mater adhering mesh (DAM).

Signal intensity of the brain tissues may present small fluctuations around the patterns exposed up to now. Any anatomical structure that is "visible" by a scanner, such as external ears or fat folds, may slightly changes an intensity variation pattern.

---

[1] A triangle with brighter signals is the one that contains samples with signal intensity at the 70th percentile of the intensities of all projected triangle samples in the ray length of 50mm. In our tests, 12 uniformly spaced points in barycentric coordinates in each triangle are sufficient for this evaluation.

Fortunately, most fluctuations have only local impacts and appear as outliers when they are rendered. We simply remove these outliers by averaging the coordinates of each vertex and its adjacent vertices after each deformation stage.
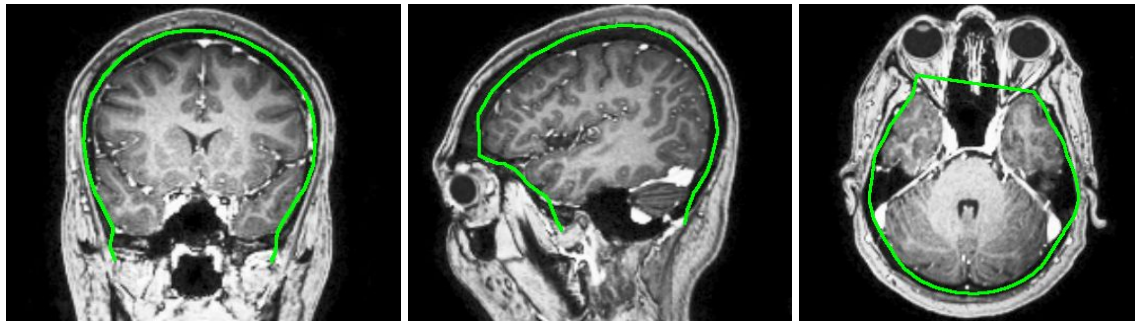
Clipping volume

Provided clipping meshes, a clipping volume that reveals the veins and cerebral convolution is created using the mesh that adheres to the scalp (SFM) and the mesh at the depth of dura-mater (DAM). Since SFM and DAM have the same topology, we simply traverse their boundaries clockwise and connect pairwise the vertices on the border of two meshes sequentially. Defined a clipping volume, rendering a curvilinearly sliced head is reducible to a volume crop problem, for which Weiskopf et al. [15] have already presented a GPU-based solution.

Results and Discussion

We implemented the proposed algorithm in C++ on top of the half-edge data structure [9]. The OpenGL shading language was employed for programming the graphics processing unit (GPU) [12]. On a desktop Intel R Core i7 2.8 GHz with 8GB of RAM and graphic card NVIDIA GTX 650Ti with 1GB of VRAM spends our algorithm less than 2s to curvilinearly reformat a volume of dimensions $180 \times 240 \times 240$. In this Section, its ability in conveying vascular and anatomical spatial relationship are assessed.

Cropping Quality

Because reconstructed volumes are tri-linearly interpolated from the scanned slices, it is enough to assess the intersection of the scanned slices with the estimated DAM. For each volume, 2D images of the intersection of DAM and the scanned images are rendered for visually checking per slice the distance of DAM to the cortical surface. Fig. 8 illustrates the analyzed images with the DAM rendered in green. If the DAM does not cross the cortical surface in all rendered images, we consider that the volume passes the validation test. In our experiment, all 3-Tesla T1wMR and GAD-T1wMRI test volumes passed the test.

(a)   Coronal   (b) Sagittal   (c) Axial

Fig. 8: Intersection of dura-mater adhering mesh (DAM) in green with T1wMR slices.

In sequence, we built the clipping volume with the estimated DAM for rendering the 3D view of cropped volumes, in order to assess its usefulness in conveying the vascular and cortical spatial relationships. We observed that not all vessels of the complex cerebral vascular system are visible. This led us to further investigate whether the visible vessels on the rendered images of cropped GAD-T1wMRI volumes suffice to provide a reliable reference system for the correspondence between preoperative and intraoperative views of brain structures.
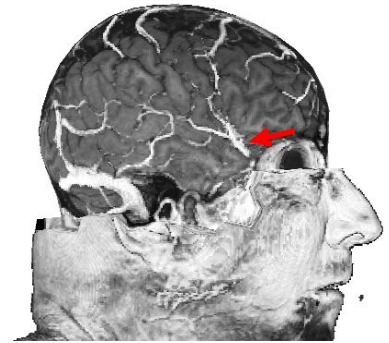
Anatomic Landmarks

Frontal veins, superior sagittal sinus, Sylvian veins, transverse sinus, superior anastomotic vein (vein of Trolard), inferior anastomotic vein (vein of Labbé) are the most relevant cerebral vascular landmarks. Those large veins and its relations to sulci and gyri are fundamental for localizing eloquent and pathological related gyri. Our evaluation tests show these large veins are among the veins displayed in cropped GAD-T1wMRI volumes. Note in Fig. 9 that some of them are not visible in their entirety. Nevertheless, they can still serve as surface landmarks for locating more accurately cerebral lesions or tumors. In addition, superficial small veins of paramount importance to localize subtle lesions are also visible over the brain parenchyma. This is the advantage of our proposal over the known angiography techniques, which are acquired separately from the brain parenchyma and need to be fused when co-localization is demanded. Our proposal is free from co-registration uncertainties.
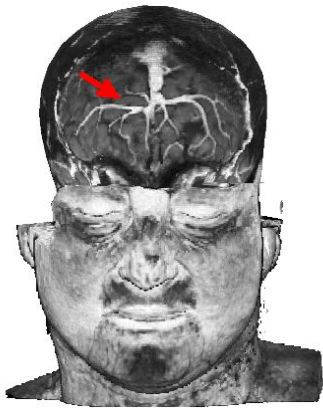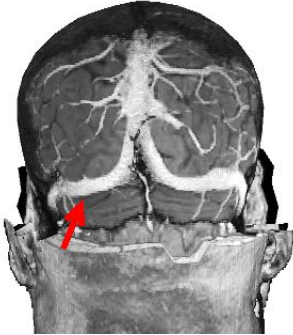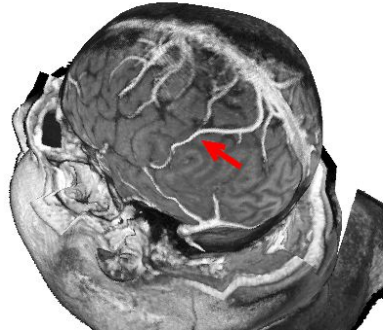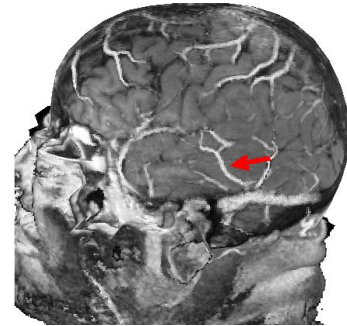
| (a) Frontal veins | (b) Superior sagittal sinus | (c) Superficial Sylvian vein |
| (d) Transverse sinus | (e) Vein of Trolard | (f) Vein of Labbé |

Fig. 9: Superficial cortical veins, pointed by the red arrows, as anatomic landmarks.

Surgical Planning

Twenty patients (9 males) with the average age of 47 years had their surgical operations done according to institution protocol (neuronavigation system) and the surgical field of all patients recorded with photos. We manually overlay these photos on the rendered preoperative cropped volumes, in order to visually assess the discrepancies between preoperative 3D GAD-T1wMRI and intraoperative surgical field. In all analyzed cases, the discrepancies between them are very subtle, suggesting reliability and usefulness of our tool for neurosurgical planning. The subject shown in Fig. 10 has pharmacoresistant temporal epilepsy with suspicious focal cortical dysplasia on a very limited circled area. The lesion could not be identified at the surgical field even under magnification. Recognizing preoperatively small veins surrounding the suspect area of cortical dysplasia increased surgeon´s certainty. Fig. 10(b) shows the extent of the resection with outcome Engel IIa.

| (a) photo overlaid on rendered image | (b) right temporal resection |

Fig. 10: Right temporal lesion in a patient with refractory epilepsy.

Table I summarizes the pathology of evaluated cases. Five cases where lesions are not visible to the naked eye intraoperatively are detailed in the electronic supplementary material[2].

Pathology	No. (%)
Ganglioglioma	1 (5%)
Low grade glioma	3 (15%)
Brain metastasis	5 (25%)
Focal cortical dysplasia	3 (15%)
High grade glioma	4 (20%)
Neurocysticercosis	1 (5%)
Pineocytoma	1 (5%)
Cavernoma	1 (5%)
Astrocitoma	1 (5%)

Table 1: Evaluated cases.

---

[2] Electronic supplementary material accompanying this manuscript.

Conclusions

Although CMPR is well-known useful tool for the diagnosis of subtle cortical lesions, we show the way that Loos et al. [8] proposed to peel off the calvaria makes CMPR also appropriate for visualizing preoperatively vascular and cortical spatial relations from GAD-T1wMRI volumes. To support a variety of views a neurosurgeon may have in craniotomy procedures, we improved their algorithm by completely removing the skull in the supratentorial compartment. The neuroanatomy knowledge has been helpful in deepening our insight into the scanned signals and in simplifying numerical processing without compromising the quality of results.

This opens new perspectives not only to improve neurosurgical planning but also to integrate the diagnosis stage with the presurgical planning in a common visual analytics environment. In developing countries where the access to state-of-the-art health technology is not always available, our free prototype available in VMTK-Neuro [16] could be a resourceful, multipurpose tool to help detection of lesions and improve the safety in complex neurosurgery.

Our algorithm requires that the MRI acquisition covers the entire head. All reported results used images from a 3 Tesla T1wMRI scanner. However, in practice, we found that several clinical studies are still scanned with 1.5 Tesla machines and most of them without the rounded top of the calvaria. As further work, we plan to validate our algorithm with 1.5 Tesla imaging exams, as well as the incomplete scans, in the domain of processable T1wMRI sequences of our algorithm.

Acknowledgments

Compliance with ethical standards

Conflict of interest The authors declare that they have no conflict of interest.

Ethical approval For this type of study, formal consent is not required.

Informed consent The volunteers enrolled in the present study signed an informed consent form approved by the Ethics Committee of University of Campinas.

References

1. Bastos, A. C., Comeau R. M., Andermann, F., Melanson, D., Cendes, F., Dubeau, F., Fontaine, S., Tampieri, D., and Olivier, A. (1999). Diagnosis of Subtle Focal Dysplastic Lesions: Curvilinear Reformatting from Three-Dimensional Magnetic Resonance Imaging, Annals of Neurology, vol. 46, no. 1, pp. 88–94.

2. Bi, W.L., Brown, P.A., Abolfotoh, M., Al-Mefty, O., Mukundan, S., Dunn, I.F. (2015). Utility of dynamic computed tomography angiography in the preoperative evaluation of skull base tumors. Journal of Neurology, vol. 123, no. 1, pp. 1-8.

3. Gering, D. T., Nabavi, A., Kikinis, R., Hata, N., O'Donnell, L. J., Grimson, W. E., Jolesz, F. A., Black, P. M., Wells, W. M. (2001). An integrated visualization system for surgical planning and guidance using image fusion and an open MR. Journal of Magnetic Resonance Imaging, 13(6): 967–975. doi:10.1002/jmri.1139.

4. Hamid, O.A., Hasaballah, M. S., Hamdy, T. A. H. (2014). The lower border of the zygomatic arch could be a better landmark for the middle fossa dura: Cadaveric dissection study. Egyptian Journal of Ear, Nose, Throat and Allied Sciences, 15(3): 177-181. doi:10.1016/j.ejenta.2014.06.004.

5. Huempfner-Hierl, H., Bohne, A., Schaller, A., Wollny, G., Hierl, T. (2015). Does facial soft tissue protect against zygomatic fractures? Results of a finite element analysis. Head & Face Medicine, 11(1). doi: 10.1186/s13005-015-0078-5.

6. Huppertz, H.J., Kassubek, J., Altenmüller, D.M., Breyer, T., Fauser, S. (2008). Automatic curvilinear reformatting of three-dimensional MRI data of the cerebral cortex. NeuroImage 39(1), 80–86.

7. Iglesias, J.E., Liu, C.Y., Thompson, P.M., Tu, Z. (2011). Robust brain extraction across datasets and comparison with publicly available methods. IEEE Trans. Med. Imaging 30(9), 1617–1634.

8. Loos, W.S., Yasuda, C.L., Cendes, F., Wu, ST. (2017). Cortical Envelope Modeling for Interactive Patient-Customized Curvilinear Reformatting in the Native Space. In: Cardoso M. et al. (eds) Imaging for Patient-Customized Simulations and Systems for

Point-of-Care Ultrasound. BIVPCS 2017, POCUS 2017. Lecture Notes in Computer Science, vol 10549. Springer, Cham.

9. Mäntylä, M. (1987). An Introduction to Solid Modeling. Computer Science Press Inc., New York.

10. Moringlane, J. R., Bartylla, K., Hagen, T., Waziri, A. (1997). Stereotactic neurosurgery planning with 3-D spiral CT-angiography. Minim Invasive Neurosurg. 40:83–86. doi:10.1055/s-2008-1053422.

11. Nowell, M., Sparks, R., Zombori, G., Miserocchi, A., Rodionov, R., Diehl, B., Wehner, T., White, M., Ourselin, S., McEvoy, A., Duncan, J. (2016). Resection planning in extratemporal epilepsy surgery using 3D multimodality imaging and intraoperative MRI. Br J Neurosurg. 31(4):468-470. doi:10.1080/02688697.2016.1265086.

12. Sellers, G., Wright, R.S., Haemel, N. (2015). OpenGL Superbible: Comprehensive Tutorial and Reference, 7th edn. Addison-Wesley Professional, Toronto.

13. Smith, S.M. (2002). Fast robust automated brain extraction. Hum. Brain Mapp. 17(3), 143–155. http://dx.doi.org/10.1002/hbm.10062.

14. Tubbs, R. S., O'Neil, J. T., Key, C. D., Zarzour, J. G., Fulghum, S. B., Kim, E. J., Lyerly, M., Shoja, M. M., Salter, E. G. and Oakes, W. J. (2007). Superficial temporal artery as an external landmark for deeper-lying brain structures. Clin. Anat., 20: 498–501. doi:10.1002/ca.20363.

15. Weiskopf, D., Engel, K., Ertl, T. (2003). Interactive clipping techniques for texture-based volume visualization and volume shading. IEEE Transactions on Visualization and Computer Graphics 9, 3, 298–312. doi:10.1109/TVCG.2003.1207438. 3, 8.

16. VMTK-Neuro(2017).http://www.dca.fee.unicamp.br/projects/mtk/vmtk-neuro/index.html. Accessed 26 February 2018.

17. Wu, S.T., Valente, A.C., de Souza Watanabe, L., Yasuda, C.L., Coan, A.C., Cendes, F. (2014). Pre-alignment for Co-registration in Native Space. In: 2014 27th SIBGRAPI Conference on Graphics, Patterns and Images, pp. 41–48.

18. Wu, S.T., Yasuda, C.L., Cendes, F. (2012). Interactive curvilinear reformatting in native space. IEEE Trans. Visual. Comput. Graph. 18(2), 299–308.